Enhanced photocatalytic activities under visible light of double-perovskite oxide semiconductor Ba$_2$Tb(Bi, Sb)O$_6$ with mixed-valence

Dayal Chandra Roy[1], Michiaki Matsukawa[1],[*] , Takanori Yonai[1], Minami Arakida[1], Haruka Taniguchi[1], Kazume Nishidate[1], Sumio Aisawa[1], Akiyuki Matsushita[2], and Lin Shiqi[2]

[1] *Faculty of Science and Engineering, Iwate University, Morioka 020-8551, Japan*
[2] *National Institute for Materials Science, Tsukuba 305-0047, Japan*

ABSTRACT

In this study, we showed the effect of Sb substitution on lattice structures, physical properties and photocatalytic activities for the double-perovskite oxides with mixed valence. High quality powders of Ba$_2$Tb(Bi$_{1-x}$Sb$_x$)O$_6$ ($0.1 \leq x \leq 1.0$) were successfully synthesized using a citrate pyrolysis approach. Through partial substitution of Sb at Bi site of this compound, it was possible to design oxidative photocatalysts at lower x, and reduction-type ones at higher x. These findings are discussed on the basis of the conduction and valence band edge potentials of a series of Ba$_2$(Tb, Pr)(Bi, Sb)O$_6$ photocatalysts. The Sb substituted sample with the $x = 0.6$ composition predicted from the machine learning procedure exhibited the highest performance of methylene blue degradation, which is comparable to typical degradation rates for good perovskite catalysts.

1 Introduction

Pseudo-cubic perovskite oxides have been extensively studied in the field of solar light active photocatalysis for water splitting into H$_2$ and O$_2$ evolution as alternative materials for TiO$_2$ [1–4]. In this crystal structure of ABO$_3$, the larger and smaller cations occupy the A and B sites, respectively. The perovskite structures have large potential to design novel functional materials based on the selective occupancy of cations at the A and B sites. Although there are so many reports on the photocatalytic properties for these candidate oxides, detailed studies on these compounds have been desired for higher performances under visible light illumination.

Double-perovskite-based oxides with the general formula AA'BB'O$_6$ provide a wider possibility to design various kinds of functional materials by tuning suitable cations at AA' and/or BB' sites. In particular, the double-perovskite-based compounds with B-site substitution belonging to A$_2$BB'O$_6$ have been investigated because of a variety of the physical

Ⓩ Springer

properties and potential applications [5]. Recently, rare-earth double-perovskites Ba_2LnBiO_6 (Ln: rare-earth element) have been examined on the view point of photocatalysis materials [6]. In particular, it is shown that the Ba_2PrBiO_6 semiconductor exhibits good performance, which is related to the mixed valence state of rare-earth ion [6, 7]. Furthermore, the magnetic susceptibility data for the Ba_2PrBiO_6 compound revealed that the average valences of Pr ion reach the intermediate values between trivalent and tetravalent states [8].

For fabrication of visible light driven photocatalysts, it is one of the key factors to tailor the energy band gap separating between the valence band (VB) and conduction band (CB) of their semiconductors [9, 10]. Moreover, it is of importance to adjust a relative relation between the upper VB and lower CB positions, and surface redox reactions in photocatalysis [11]. It is needed that the absolute positions of the VB and CB edges are optimized to effectively facilitate photocatalytic oxidation and reduction processes. Our goal of higher photocatalytic activity is achieved by reducing the rapid recombination of electrons and holes and promoting the photo-excited charge separation, before the redox reaction at the surface [9, 12]. In our previous research [13], it has been proposed that the coexistence between Pr^{3+} and Pr^{4+} ions contributes to the separation of photogenerated charge carries. Further, we extended photocatalytic researches to the Ba_2TbBiO_6 system [14].

In this paper, we demonstrate crystal structures, physical, and photo-active properties for $Ba_2Tb(Bi_{1-x}Sb_x)O_6$, for our further understanding of photocatalytic activities of double-perovskite compounds with mixed valence states. First, the experimental setups are briefly illustrated. In the section of results and discussion, we describe the structural phase diagram, the mixed valence states, and the energy band gaps for the $Ba_2Tb(Bi_{1-x}Sb_x)O_6$. system, on the basis of tolerance factors, and band calculations. For both the Pr- and Tb-based compounds, we evaluate the photocatalytic activities of the MB reductive degradation and the 2-propanol oxidative decomposition as a function of band gap energy. Furthermore, these findings are well explained in terms of CB and VB edge potentials of the $Ba_2(Tb, Pr)(Bi, Sb)O_6$ photocatalysts [15, 16]. For comparison, the structural, physical and photocatalytic data for $BaBiO_3$ prepared by the same approach

are given since its chemical formula $Ba_2Bi^{3+}Bi^{5+}O_6$ is taken as a pristine compound of $Ba_2Ln^{3+}Bi^{5+}O_6$ [17, 18]. Finally, the concluding section is given.

2 Experiment

High quality powders of $Ba_2Tb(Bi_{1-x}Sb_x)O_6$ with $x = 0.1, 0.1, 0.5, 0.6,$ and 1.0, and $BaBiO_3$ were synthesized using the citrate pyrolysis approach [13, 14]. In the first step, at 70–80 °C, stoichiometric mixtures of high purity $Ba(NO_3)_2$, Tb_4O_7, Bi_2O_3, and Sb were dissolved in nitric acid solution. After adding citric acid and neutralizing it with aqueous ammonia, we obtained the porous products through the self-ignition process using halogen-lamp stirrer. (Molar ratio of metal cations, citric acid, and nitric acid, $Ba_2Tb(Bi, Sb)O_6$:$C_6H_8O_7$:HNO_3 = 1:6:10.) In the next step, the precursors were ground and the resultant fine powders were annealed in air (or nitrogen gas) at 900–1000 °C for 48–96 h, in order to synthesize the double-perovskite phase. Powder X-ray diffraction data for all the samples were collected with a diffractometer (Ultima IV, Rigaku). The lattice parameters were calculated from the X-ray diffraction data using the least-squares fits [19], as listed in Table 1. The surface area of powder samples was obtained by BET measurement on N_2 absorption at 77 K (BELSORP-mini II , Microtrac). The polycrystalline films for the scanning electron microscope (SEM) measurement were fabricated from the $Ba_2Tb(Bi_{1-x}Sb_x)O_6$ powders using an electrophoretic deposition technique [20]. Typical SEM images for $Ba_2Tb(Bi_{1-x}Sb_x)O_6$ ($x = 0.5$) powders will be given in Fig. 2.

For our estimation of energy band gaps, optical measurements were conducted using a diffuse reflectance spectroscopy (V550, JASCO Co.). We applied the Kubelka–Munk (KM) conversion to the diffuse reflection spectrum and obtained the optical band gap energies by the extrapolation [6, 13, 17]. Moreover, electronic band structures for the double-perovskite structure compound $Ba_2Tb(Bi_{1-x}Sb_x)O_6$ were calculated using the density functional theory as implemented in the 'Quantum ESPRESSO' [21, 22]. We utilized the Perdew–Burke–Ernzerhof (PBE) functional [23] for the exchange-correlation effect. Pseudopotentials of 'pslibrary' [24] were adopted to represent the core electronic states. The cut off energy of 40 Ry and the $4 \times 4 \times 4$ Monkhorst–Pack grid for the K-point sampling were applied.

Table 1 Structural and physical properties, and photocatalytic performance for $Ba_2Tb(Bi_{1-x}, Sb_x)O_6$.

Sb x	Crystal symmetry	a (Å)	b (Å)	c(Å)	μ_{eff} (μ_B)	E_g (eV)	CO_2 (ppm/g)	MB (%)
0.0	Monoclinic	6.1223[a]	6.0903	8.6110	8.91[a]	0.92[a]	221	9.7[a]
0.1	Monoclinic	6.1069	6.0809	8.5916	8.89	0.94	204	–
0.5	Cubic	8.4814[a]	–	–	8.86[a]	2.45[a]	32	80.7[a]
0.6	Cubic	8.4611	–	–	9.13	2.59	–	85.8
1.0	Cubic	8.4506	–	–	–	–	–	81.3
$BaBiO_3$	Monoclinic	6.1910	6.1407	8.6780	–	0.83[b] 2.10[c]	–	10.7

Crystal symmetry, lattice parameters, effective magnetic moment, energy gap, gas evolution of CO_2, and MB degradation are summarized for $x = 0.0, 0.1, 0.5, 0.6$ and 1.0. The CO_2 and MB data for photocatalytic activities were collected at an irradiation time of 90 min and 60 min, respectively. For comparison, the data for $BaBiO_3$ prepared by the citrate method are given, which will be also shown in Figs. S1 and S2

[a]Reference [14]

[b]Indirect

[c]Direct

For our understanding of the valence state of Tb ion, we estimated the values of effective magnetic moment (μ_{eff}) through applying the Curie–Weiss law to the magnetic susceptibility data. Here, the temperature variation of dc magnetization was measured under the magnetic field cooling process of 0.1 T using a superconducting quantum interference device magnetometer (MPMS, Quantum Design).

Finally, we demonstrated the methylene blue (MB) degradation as a function of the Sb content, to evaluate photocatalytic reduction performance of the $Ba_2(Tb, Pr)(Bi_{1-x}Sb_x)O_6$ fine powders. A 300 W Xe lamp system including UV and IR filters was utilized as the light source (Cermax LX300F, Excelitas Technologies). In reducing environment, it is a common understanding that aqueous MB is decolorized to colorless leuco-MB, LMB [25, 26], and it has been widely used for the model pollution. The MB aqueous solution of 50 mL (10 ppm) and $Ba_2(Tb, Pr)(Bi, Sb)O_6$ powders of 0.2 g were prepared . Before visible light irradiation, the suspension of the photocatalyst powders was stirred in the dark for 30 min. We measured the temporal bleaching of MB with the UV–Vis spectrometer (V730, JASCO Co.). The MB solution of 3 mL was transferred into the test cell for chemical analysis at the regular time interval. For comparison, we examined the photo-induced decomposition of 2-propanol (IPA) using a gas chromatography system (GC-2014, Shimadzu Co.). After photocatalytic oxidation of the IPA gas, the amount of resultant CO_2 was recorded as a function of time, as described in [13, 27].

3 Results and discussion

Figure 1 shows the X-ray diffraction data for the Sb substituted $Ba_2Tb(Bi_{1-x}Sb_x)O_6$ compounds. Typical SEM image of the cubic $Ba_2Tb(Bi_{0.5}Sb_{0.5})O_6$ is shown in Fig. 2. The polycrystalline grains with sub-micron order were uniformly distributed on the surface of electrophoretical deposition film. A SEM photograph for the Sb-free sample has been presented in [14]. Furthermore, the morphologies for the Ba_2PrBiO_6 ($x = 0$) and the Sb substituted $Ba_2Pr(Bi_{1-x}Sb_x)O_6$ ($x = 0.1$ and 1.0) have been examined in Fig. 2a in [13] and Fig. S2a and b in [13], respectively. These experimental data revealed that the Sb substitution at Bi sites promotes the refinement of polycrystalline grains. This fact seems to be close to good performance of photocatalysis as well as other factors, as will be discussed later.

The lower Sb substituted sample was well fitted on the basis of monoclinic structure model as the parent sample [14]. The samples with higher Sb contents ($0.5 \leq x \leq 1.0$) crystallized in a cubic phase. The lattice parameters estimated for the end-member $x = 1.0$ sample were in good agreement with previous data [8, 28]. In Fig. 3, the structural parameters for all the samples are plotted as a function of Sb content, which are also listed in Table 1.
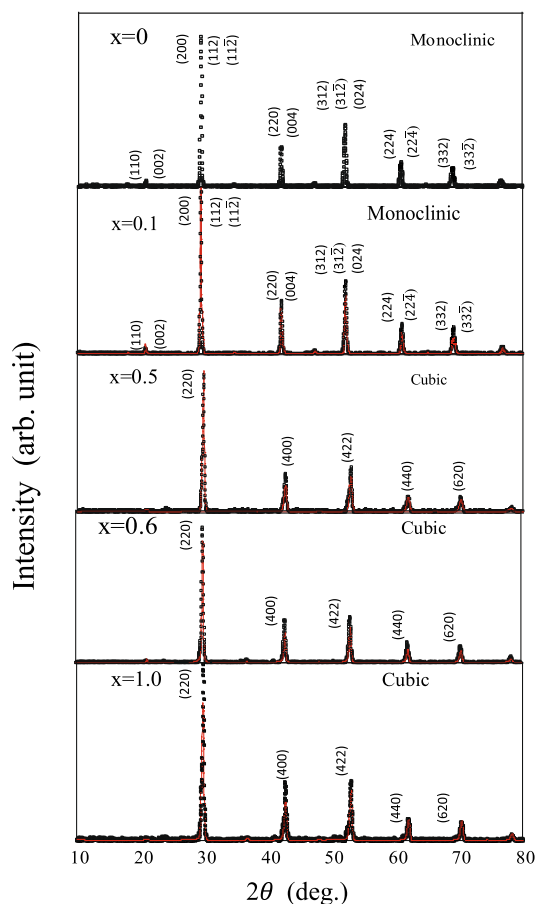
Fig. 1 Powder X-ray diffraction data (black dots) for the monoclinic $Ba_2Tb(Bi_{1-x}Sb_x)O_6$ ($x = 0.0$ and 0.1) and cubic $Ba_2Tb(Bi_{1-x}Sb_x)O_6$ ($0.5 \leq x \leq 1.0$). X-ray diffraction curves (red lines) were computed using the corresponding lattice parameters, which will be given in Table 1 (Color figure online)
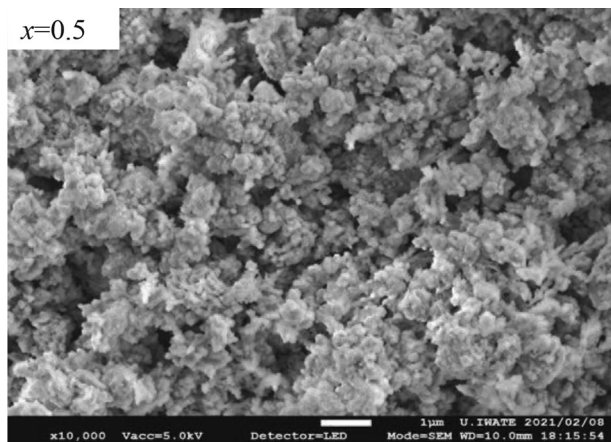

Fig. 2 SEM image of the cubic $Ba_2Tb(Bi_{0.5}Sb_{0.5})O_6$

For our understanding of the valence state of Tb ion, we estimated the values of effective magnetic moment (μ_{eff}) through applying the Curie–Weiss law to the magnetic susceptibility data (not shown). For example, we evaluated $\mu_{eff} = 8.89\ \mu_B$ at the $x = 0.1$ and $9.13\ \mu_B$ at $x = 0.6$, as listed in Table 1. Using the similar equation as described in [13, 29], the ratio of Tb^{3+} to Tb^{4+} ions is ranging from 0.51:0.49 at $x = 0$ to 0.64:0.36 at $x = 0.6$. The magnetization measurements on both the present Tb and previous Pr-based samples revealed that their mixed valence states are a common property over the whole range of the Sb content [13]. In addition, it is another evidence that X-ray photo-emission spectroscope study on the Pr-based sample has revealed a dominant peak of the trivalent ion accompanied by a shoulder structure of tetravalent ion [30].

Next, we discuss the stability of the crystallographic phase diagram in Fig. 3 using the tolerance factor considering the mixed valence state of the Tb ions. The tolerance factor for $Ba_2Tb(Bi_{1-x}Sb_x)O_6$ is given in the form of the following equation,

$$t = \frac{r_{Ba} + r_O}{\sqrt{2}\left(\frac{r_{Tb}+r_M}{2} + r_O\right)},$$

where r_{Ba}, r_O, r_{Tb}, and $r_{M=(Bi,Sb)}$ are the ionic radii of each element (in details, refer to [31]). In general, it is well-known that the tolerance factor represents a
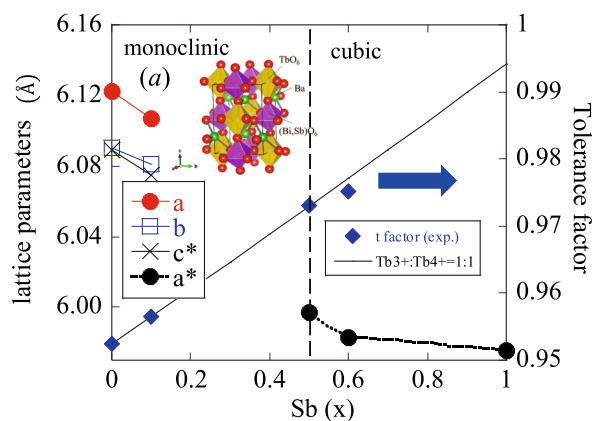

Fig. 3 Lattice parameters (left hand side) and tolerance factor (right-hand side) as a function of Sb content for $Ba_2Tb(Bi_{1-x}Sb_x)O_6$. ($c^* = c/\sqrt{2}$, $a^* = a/\sqrt{2}$). The data points for the $x = 0, 0.1, 0.5,$ and 0.6 samples show the tolerance factor estimated from the ratio of Tb^{3+} to Tb^{4+} (see the text). For comparison, a solid line denotes the tolerance factor for the mixed valence state of Tb ion ($Tb^{3+}:Tb^{4+} = 1:1$)

lattice distortion of the ABO_3 perovskite structure. As for the trivalent and tetravalent ions of Tb, we evaluated the tolerance factors using the chemical formula such as $Ba_2^{2+}Tb^{3+}Bi_{1-x}^{5+}Sb_x^{5+}O_6$ and $Ba_2^{2+}Tb^{4+}M1_{1-x}^{4+}M2_x^{4+}O_6$, respectively [14]. Here, we set $M1^{4+} = Bi_{0.5}^{3+}Bi_{0.5}^{5+}$ and $M2^{4+} = Sb_{0.5}^{3+}Sb_{0.5}^{5+}$. In Fig. 3, the tolerance factor was shown for a mixed valence state of $Ba_2^{2+}Tb_{0.5}^{3+}Tb_{0.5}^{4+}Bi_{(1-x)/2}^{5+}Sb_{x/2}^{5+}M1_{(1-x)/2}^{4+}M2_{x/2}^{4+}O_6$ ($0.0 \le x \le 1.0$). The data points for the $x = 0, 0.1, 0.5$, and 0.6 samples are displayed as their tolerance factors considering the ratio of Tb^{3+} to Tb^{4+} from the magnetic moments as mentioned before. The tolerance factor for $Ba_2Ln(Bi, Sb)O_6$ as a function of the ionic radius of Ln (Ln: rare-earth element) has been reported in [28]. The crystallographic phase diagram for the double-perovskite rare-earth compounds is separated into the monoclinic, rhombohedral, and cubic regions. The crystal structures obtained for the lower and higher Sb substituted samples are in reasonable agreement with the phase diagram reported. For the $x = 0.5$ sample, the ratio of Tb^{3+} to Tb^{4+} listed in Table 1 gives rise to the value of $t = 0.973$, which is located just above the phase boundary between cubic and rhombohedral structures [32]. This finding is related to the stability of the cubic phase for higher Sb substituted samples [33].

Here, we give some comments on the factors affecting B-site cation ordering. The charge difference between the B and B′ cation oxidation states is defined as ΔZ_B, whereas we represent the ionic radius difference between the two states as Δr_B. For the compounds with the trivalent, intermediate, and tetravalent ions of Tb, we obtain $\Delta Z_B = 2, 1$, and 0, respectively. In the case of $\Delta Z_B = 2$, the B-site cations of $A_2^{2+}B^{3+}B'^{5+}O_6$ perovskites tend to order with increasing Δr_B [5]. On the other hand, $A_2^{2+}B^{4+}B'^{4+}O_6$ perovskite compounds with $\Delta Z_B = 0$ are disordered when $\Delta r_B < 0.17$ Å. Accordingly, it is expected that the present mixed valence compounds exhibit a partially disordered phase.

Applying the KM conversion to the diffuse reflection spectrum, we obtained the typical optical spectra of the KM conversion for the $x = 0.1$ and 0.6 samples (Fig. 4). Additionally, we evaluated the optical band gap energies by the extrapolation [6, 13, 17], as shown in the inset of Fig. 4. For the direct and indirect optical transitions, we utilized the absorption coefficient $(\alpha_{KM}\varepsilon_p)^2$ vs. ε_p plot and $(\alpha_{KM}\varepsilon_p)^{1/2}$ vs. ε_p plot,

respectively (in details, see [6, 13]) . Here, α_{KM}, and ε_p represent the absorption coefficient, and the photon energy. For the Sb substituted samples, we estimated E_g to be 0.94 eV at $x = 0.1$ and 2.59 eV at $x = 0.6$, as listed in Table 1. The Sb substitution for Bi enlarges the band gap energy as well as that in the case of the Pr-based compound. Following our previous work on $Ba_2Pr(Bi_{1-x}Sb_x)O_6$ [34, 35], we examined the influence of the Sb substitution on band gap energies on the basis of first-principle electronic structure calculation. In Fig. 5, we exhibit our calculated results for both the monoclinic Ba_2TbBiO_6 and cubic Ba_2TbSbO_6 compounds. We adopted the experimentally determined lattice parameters as listed in Table 1. The atomic position parameters listed in Table 2 were used [8, 28]. Here, we utilized the density functional theory as implemented in the Quantum ESPRESSO [21, 22], to study the structural and electronic properties of the corresponding double-perovskite. The direct band gaps were evaluated to be 1.90 eV and 3.77 eV for the parent and end-member samples. Our previous findings predict that the 6s orbitals of the Bi^{5+} ion occupy the bottom of the CBs, while the top of the VBs is composed of the 6s orbitals of the Bi^{3+} ion. Accordingly, it is reasonable that Bi^{5+} is partially replaced by Sb^{5+} with increasing Sb content, resulting in the band gap
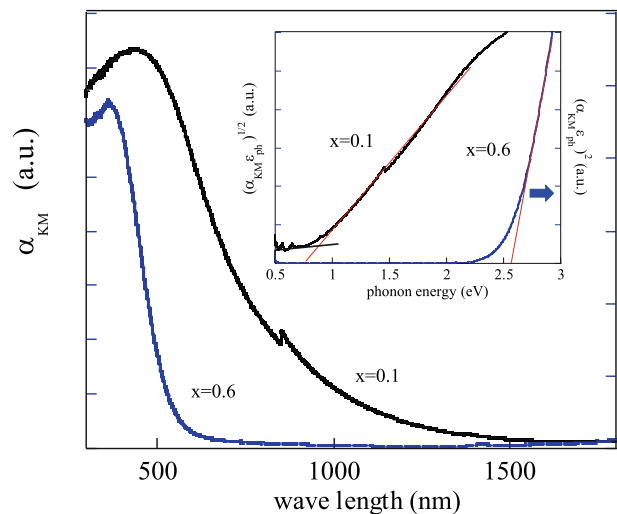
Fig. 4 KM conversion to diffuse reflection spectrum for $Ba_2Tb(Bi_{1-x}, Sb_x)O_6$ with $x = 0.1$ and 0.6. Inset shows optical band gap estimation. For $x = 0.6$, $(\alpha_{KM}\varepsilon_p)^2$ vs. ε_p plot for the direct band gap was used. For the indirect band gap, we applied plots of $(\alpha_{KM}\varepsilon_p)^{1/2}$ vs. ε_p to the inset data for the $x = 0.1$ sample. The values of E_g were given by the extrapolation method
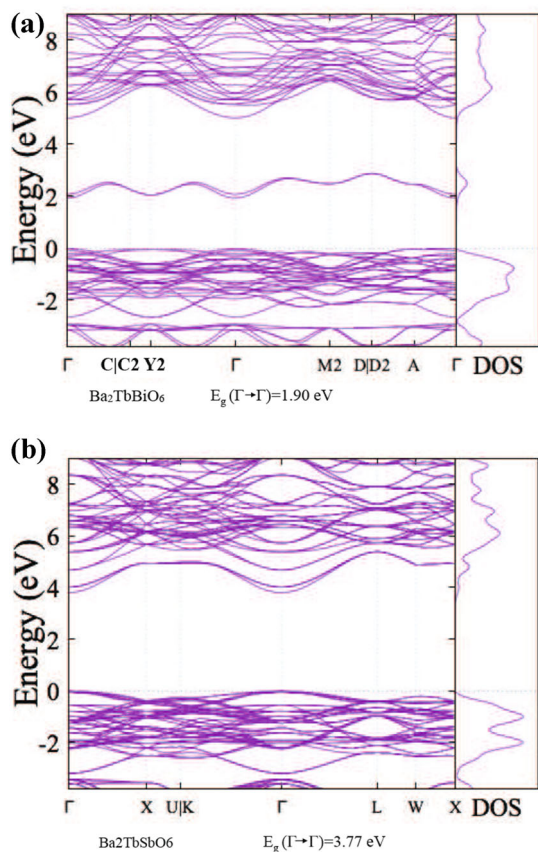
Fig. 5 Energy band structures and total density of states near the Fermi levels for **a** monoclinic Ba_2TbBiO_6 and **b** cubic Ba_2TbSbO_6. Band gap values are 1.90 eV and 3.77 eV for the former and latter compounds, respectively

Table 2 Atomic position parameters

Ba_2TbBiO_6 atom	($I2/m$) site	x	y	z
Ba	4i	0.5036	0.5	0.25
Tb	2c	0.5	0	0
Bi	2b	0	0.5	0
O1	8j	0.24210	0.25400	−0.03340
O2	4i	0.43610	0	0.25890

Ba_2TbSbO_6 atom	($Fm\bar{3}m$) site	x	y	z
Ba	8c	0.25	0.25	0.25
Tb	4b	0.5	0.5	0.5
Sb	4a	0	0	0
O	24e	0.237	0	0

opening. Furthermore, we found out that the partial B-site disordering of the double-perovskite compound $Ba_2Tb(Bi_{1−x}Sb_x)O_6$ causes narrowing the band

gaps. For the present calculation, the B-site disordering effect has not been considered, which is probably related to the overestimation of the band gap for the parent sample. For the pristine perovskite $BaBiO_3$, the optical measurement as shown in Fig. S2 revealed an indirect energy gap of 0.83 eV followed by a direct one of 2.1 eV. This result is in good agreement with the several theoretical predictions based on the density functional approach [35, 36].

Furthermore, we demonstrated the reductive degradation of methylene blue under visible light irradiation for the $Ba_2(Tb, Pr)(Bi, Sb)O_6$ citrate pyrolysis samples. Figure 6a shows the typical absorbance spectra for the MB degradation of $Ba_2TbBi_{0.4}Sb_{0.6}O_6$. When the peak intensities around $\lambda = 665$ nm are responsible for the MB concentrations, the MB degradation rate (%) is expressed as $(C(0) − C(t))/C(0) \times 100$. Here, $C(0)$ and $C(t)$ represent at the initial and final concentrations at different time intervals, respectively. In Fig. 6b, c, the MB degradation data for $Ba_2Tb(Bi_{1−x}, Sb_x) O_6$ and $Ba_2Pr(Bi_{1−x}, Sb_x) O_6$ are plotted as a function of time under visible light irradiation. The reductive degradation rates of MB to colorless LMB rapidly increased with substituting Sb at the Bi site. For the Tb-based samples with heavy Sb content, their higher performances were observed. For the $Ba_2Pr(Bi_{1−x}, Sb_x) O_6$ system, the end-member sample Ba_2PrSbO_6 exhibited highest degradation among all the Pr-based samples. Here, we comment on the reason for selecting the $x = 0.6$ composition in the Tb-based compounds. Recently, with the aid of materials informatics such as machine learning, it is possible to design new materials with the desired properties under minimum experiments or simulations [37]. We applied the machine learning program (Common Bayesian Optimization library, COMBO.exe [38]) to the three data sets (Sb content, MB degradation) obtained for the both end-member and intermediate samples ($x = 0.0, 0.5$ and 1.0). As a result of this procedure, the $x = 0.6$ composition was recommended as next candidate material. In fact, the experimental data in Fig. 6b strongly support the present prediction though there are small differences in the MB degradation rate. The band gap for the $x = 0.6$ sample showed 2.59 eV as listed in Table 1, which is slightly larger than the values for the $x = 0.5$ and 1.0 samples. Additionally, the Sb substitution at Bi sites promoted the refinement of powder samples as shown in our previous study [13]. Around $x = 0.6$, it is expected
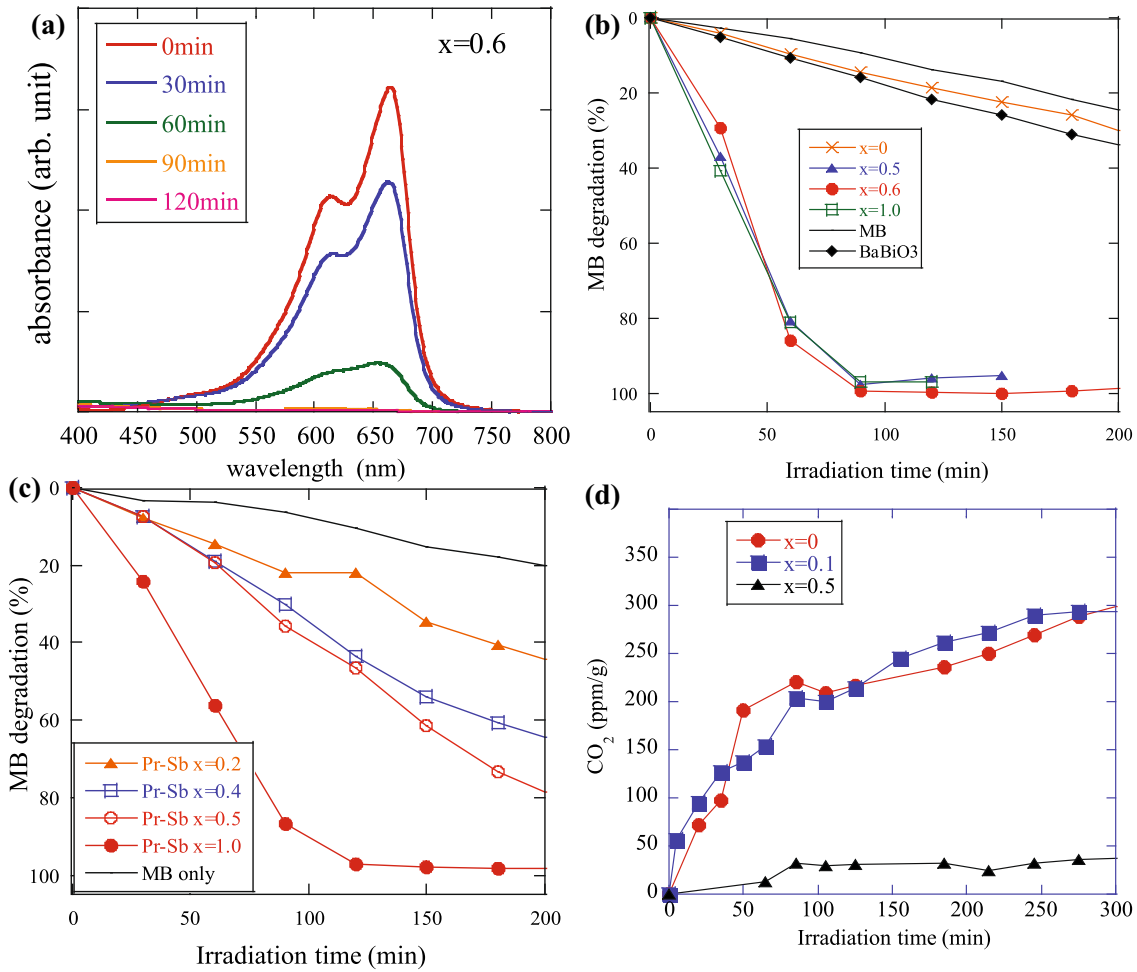
Fig. 6 a Typical absorbance spectra of MB degradation under visible light illumination for $Ba_2TbBi_{0.4}Sb_{0.6}O_6$. MB degradation vs. irradiation time for **b** $Ba_2Tb(Bi_{1-x}\ Sb_x)O_6$ and **c** $Ba_2Pr(Bi_{1-x}\ Sb_x)O_6$. The solid line denotes the MB only decomposition data. **d** Visible light driven CO_2 evolution vs. irradiation time for the $Ba_2Tb(Bi_{1-x}\ Sb_x)O_6$ powder samples. The data for the $x = 0$ and 0.5 samples prepared from the different batches were collected

that the photocatalytic active sites on the powder surfaces are optimized against the number of MB molecules. These factors contribute to the highest performance for MB degradation. Furthermore, in Table 3, the MB degradation rates for typical perovskite compounds such as manganite, titanate, ferrite and niobium perovskites were cited. Our present data seem to be comparable to other similar studies. For the pristine perovskite $BaBiO_3$ with $E_g = 0.83$ eV, we obtained low MB degradation rate similar to that of the Ba_2TbBiO_6. Compared with the previous studies on $BaBiO_3$ [17, 18], we note that the present sample is isostructural with the previous one provided by Tang. However, the latter sample with a relatively larger gap of 2.05 eV exhibited high photocatalytic performance of MB degradation as listed

in Table 3. The discrepancies in the energy band gap and its associated photo-induced activity are probably related to partial B-site disordering. Additionally, the photo-induced reaction on the surface of powders strongly depends on sample synthesis approaches [18].

In addition to the MB degradation, we examined the photocatalytic oxidation activity of the powder samples using gaseous 2-propanol (IPA). Figure 6d shows the visible light driven CO_2 evolution vs. irradiation time for the $Ba_2Tb(Bi_{1-x},\ Sb_x)\ O_6$ powder samples. The CO_2 concentration for the samples with light Sb content showed a rapid enhancement at the initial time and then remained a steady rise at further irradiation time. This stable behavior is responsible for the CO_2 absorption process on the surface of the

Table 3 Comparison with different perovskite photocatalysts for MB degradation rate

Catalyst	Initial MB (mg/L)	Mass (mg)	Time (min)	Degradation rate (%)
$Ba_2Tb(Bi, Sb)O_6$	10	200	90	100
$BaBiO_3$ [17]	15.3	300	60	100
$Nd_{0.7}Ca_{0.3}MnO_3$ [39]	10	40	180	96
Fe-doped $CaTiO_3$ [40]	10	100	180	100
Y-doped $BiFeO_3$ [41]	50	100	120	97.6
$NaNbO_3$ [42]	10	160	180	99.3

powders, leading to a reduction of the photo-induced CO_2 gas concentration. For the $x = 0.5$ sample, we detected no remarkable quantity of CO_2.

Our photocatalytic data for both the MB degradation and IPA decomposition are scaled with the band gap energy in Fig. 7a. The data for CO_2 evolution and MB decomposition rate were collected at a light irradiation time of 90 min. The unit for CO_2 concentration was transformed by the BET surface area of the samples. For both the Pr- and Tb-based compounds, we conclude that the photocatalytic reduction process of MB bleaching is in contrast to the oxidative one of IPA decomposition with respect to the magnitudes of band gap energy.
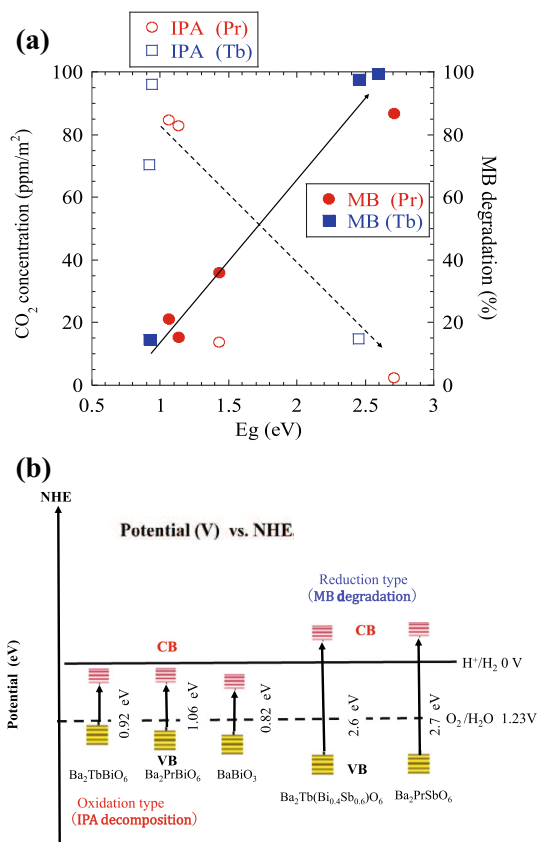
In Fig. 7b, we illustrate schematic plot of the band edge potential with respect to normal hydrogen electrode (NHE) for the $Ba_2(Tb, Pr)(Bi, Sb)O_6$ compounds. For the Sb-free compounds, their VB edge potentials are located to facilitate oxidation reaction. However, the lower CB level is not suitable for promoting reduction reaction. On the other hand, the higher CB edge potentials for both $Ba_2Tb(Bi_{0.4}Sb_{0.6})O_6$ and $Ba_2PrSb O_6$ are suitable for promoting effective reduction process. Here, the CB edge potential (E_{CB}) of the $Ba_2(Tb, Pr)(Bi, Sb)O_6$ semiconductor is estimated using the following empirical equation [15, 16],

$$E_{CB} = \chi - E^e - 0.5E_g,$$

where χ and E^e are the electronegativity of the semiconductor and the energy of free electrons on the hydrogen scale (~ 4.5 eV), respectively. For example, the electronegativity of the present $Ba_2Tb(Bi_{1-x}, Sb_x)O_6$ semiconductor is calculated by the geometric average of the electronegativities of its constituent atoms in the following form [16, 17],

$$\chi = [\chi^2(Ba)\chi(Tb)\chi^{1-x}(Bi)\chi^x(Sb)\chi^6(O)]^{1/10},$$

where the atomic electronegativity on the right-hand side is given by the arithmetic average of the atomic electron affinity and the first ionization energy [15].

Fig. 7 **a** Photocatalytic activity vs. band gap energy. The published data for $Ba_2Pr(Bi_{1-x} Sb_x)O_6$ are referred from our previous work [13, 14]. **b** Schematic illustration of the band edge potential with respect to normal hydrogen electrode (NHE) for $Ba_2(Tb, Pr)(Bi, Sb)O_6$ and $BaBiO_3$ compounds

According to this expression, we evaluated the CB edge potential E_{CB} to be 0.34 eV and -0.45 eV for the parent and $x = 0.6$ substituted samples, respectively. In a similar way, for the Pr-based photocatalytic end-member compounds, the values of E_{CB} were estimated to be 0.23 eV at $x = 0.0$ and -0.51 eV at $x = 1.0$. For the parent compounds with $E_g \sim 1$ eV, the oxidation reactions concerning the IPA decomposition process are in progress through the photo-excited holes near the VB edge. The heavily Sb

substituted compounds with $E_g \sim 2.5$ eV exhibit the strong degradation of MB and their CB edges are optimized for the photocatalytic reductive reactions.

Finally, we give some comments on the mixed valence states. As mentioned in Introduction, the mixed valence states between trivalent and tetravalent rare-earth ions are related to the improvement in photogenerated charge separation. In addition, the ionic radius differences between trivalent and tetravalent ones give rise to the B-site partial disordering and then suppress the band gap energies of the ordered double-perovskite compounds. Moreover, for the highly Sb substituted samples, their mixed valence states contribute to the stability of the cubic phase through the higher tolerance factors as discussed above.

4   Conclusion

We investigated the influence of Sb substitution at B sites on the lattice structures, the magnetic valence states, the band gap energies, and photocatalyst performance for the double-perovskite-based semiconductors. High quality powders of $Ba_2Tb(Bi_{1-x}Sb_x)O_6$ $(0.1 \leq x \leq 1.0)$ were successfully synthesized using the citrate pyrolysis approach. The single-phase powder samples with the light and heavy Sb contents crystallized in the monoclinic and cubic structures, respectively. These findings are in reasonable agreement with the structural phase diagram previously reported, through the tolerance factor considering the mixed valence states. We examined the band gap widening associated with the partial substitution of Sb through performing the optical reflectance measurement and first-principle electronic structure calculation.

Through the partial substitution of Sb at Bi site of this compound, it was possible to design oxidative photocatalysts at lower x, and reduction-type ones at higher x. The photocatalytic properties were well explained in terms of CB and VB edges of the Ba_2(Tb, Pr)(Bi, Sb)O_6 photocatalysts. For the $x = 0.6$ sample, we experimentally observed the highest performance of MB degradation, which was derived from the machine learning prediction. These data seem to be comparable to typical degradation rates for good perovskite catalysts. For comparison, the structural, physical and photocatalytic data for $BaBiO_3$ synthesized by the same approach were shown since its chemical formula $Ba_2Bi^{3+}Bi^{5+}O_6$ was considered as a pristine compound of double-perovskite oxide semiconductor.

Author contributions

DCR: Material preparation, Data collection and analysis, Writing—Original draft preparation. MM: Writing—Reviewing and Editing, Supervision, Project administration, Funding acquisition. TY: Material preparation, Data collection. MA: Material preparation, Data collection. HT: Data analysis. KN: Data analysis, Conceptualization, Funding acquisition. SA: Methodology. AM: Conceptualization, Methodology. LS: Data collection.

Data availability

Data will be made available on request.

Declarations

Conflict of interest On behalf of all authors, the corresponding author states that there is no conflict of interest.

Supplementary Information: The online version of this article (https://doi.org/10.1007/s10854-022-09542-6) contains supplementary material, which is available to authorized users.

References

1. J. Shi, L. Guo, Prog. Nat. Sci. Mater. Int. **22**, 592–615 (2012)
2. P. Kanhere, Z. Chen, Molecules **19**, 19995–20022 (2014)
3. E. Grabowska, Appl. Catal. B **186**, 97–126 (2016)
4. A. Fujishima, K. Honda, Nature **238**, 37–38 (1972)
5. S. Vasala, M. Karppinen, Prog. Solid State Chem. **43**, 1–31 (2015)
6. T. Hatakeyama, S. Takeda, F. Ishikawa, A. Ohmura, A. Nakayama, Y. Yamada, A. Matsushita, J. Yea, J. Ceram. Soc. Jpn **118**, 91–95 (2010)
7. A. Matsushita, T. Nakane, T. Naka, H. Isago, Y. Yamada, Jpn. J. Appl. Phys. **51**, 121802-1-5 (2012)
8. W.T.A. Harrison, K.P. Reis, A.J. Jacobson, L.F. Schneemeyer, J.V. Waszczak, Chem. Mater. **7**, 2161–2167 (1995)
9. X. Chen, S. Shen, L. Guo, S. Mao, Chem. Rev. **110**, 6503–6570 (2010)
10. D. Sudha, P. Sivakumar, Chem. Eng. Process. **97**, 112–133 (2015)
11. H.W. Eng, P.W. Barnes, B.M. Auer, P.M. Woodward, J. Solid State Chem. **175**, 94–109 (2003)
12. B. Ohtani, Catalysts **3**, 942–953 (2013)
13. A. Sato, M. Matsukawa, H. Taniguchi, S. Tsuji, K. Nishidate, S. Aisawa, A. Matsushita, K. Zhang, Solid State Sci. **107**, 10635-1-7 (2020)
14. T. Senzaki, M. Matsukawa,T. Yonai, H. Taniguchi, A. Matsushita,T. Sasaki, M. Hagiwara, Chap. 9. In: *Functional Materials Synthesis and Physical Properties*, ed by M. Bartoli (IntechOpen, 2022). https://doi.org/10.5772/intechopen.100241.
15. A.H. Nethercot, Phys. Rev. Lett. **33**, 1088–1091 (1974)
16. M.A. Butter, D.S. Ginley, J. Electrochem. Soc. **125**, 228–232 (1978)
17. J.W. Tang, Z.G. Zou, J.H. Ye, J. Phys. Chem. C **111**, 12779–12785 (2007)
18. B. Men, J. Zhang, C. Diao, X. Liu, H. Zheng, J. Mater. Sci. Mater. Electron. **111**, 12779–12785 (2018)
19. F. Izumi, K. Momma, Solid State Phenom. **130**, 15–20 (2007)
20. M. Kawachi, N. Sato, E. Suzuki, S. Ogawa, K. Noto, M. Yoshizawa, Physica C **357–360**, 1023–1026 (2001)
21. P. Giannozzi et al., J. Phys. Condens. Matter **21**, 395502 (2009)
22. P. Giannozzi et al., J. Phys. Condens. Matter **29**, 465901 (2017)
23. J.P. Perdew, K. Burke, M. Ernzerhof, Phys. Rev. Lett. **77**, 3865–3868 (1996)
24. A. Dal Corso, Comput. Mater. Sci. **95**, 337–350 (2014)
25. W.S. Wang, N. Xie, L. He, Y.D. Yin, Nat. Commun. **5**, 5459-1-7 (2014)
26. Y.N. Liu, X. Zhou, X. Wang, K. Liang, X.K. Yang, C.C. Shen, M. Imran, S. Sahar, A.W. Xu, RSC Adv. **7**, 30080–30085 (2017)
27. T. Murase, H. Irie, K. Hashimoto, J. Phys. Chem. B **108**, 15803–15807 (2004)
28. S. Otsuka, Y. Hinatsu, J. Solid State Chem. **227**, 132–141 (2015)
29. We estimated the ratio (y) by using $\mu_{\text{eff}}^2 = y\mu_{\text{eff}}^2(\text{Tb}^{3+}) + (1 - y)\mu_{\text{eff}}^2(\text{Tb}^{4+})$ with $\mu_{\text{eff}}(\text{Tb}^{3+})$=9.72 μ_B and $\mu_{\text{eff}}(\text{Tb}^{4+})$=7.94 μ_B
30. K. Onodera, T. Kogawa, M. Matsukawa, H. Taniguchi, K. Nishidate, A. Matsushita, M. Shimoda, J. Phys. Conf. Ser. **969**, 012122-1-6 (2018)
31. R. Shannon, Acta Crystallogr. A **32**, 751 (1976)
32. W.T. Fu, D.J.W. Ijdo, J. Solid State Chem. **178**, 2363–2367 (2005)
33. P.J. Saines, B.J. Kennedy, M.M. Elcombe, H.H. Harris, L.Y. Jang, Z. Zhang, J. Solid State Chem. **181**, 2941–2952 (2008)
34. H. Taniguchi, M. Matsukawa, K. Onodera, K. Nishidate, A. Matsushita, IEEE Trans. Magn. **55**, 2400404-1-4 (2019)
35. K. Nishidate, A. Adiko, M. Matsukawa, H. Taniguchi, A. Sato, A. Matsushita, S. Tanibayashi, M. Hasegawa, Mater. Res. Express **7**, 065505-1-8 (2020)
36. C. Franchini, A. Sanna, M. Marsman, G. Kresse, Phys. Rev. B **81**, 085213-1-7 (2010)
37. R. Tamura, T. Osadab, K. Minagawa, T. Kohata, M. Hirosawa, K. Tsuda, K. Kawagishi, Mater. Des. **198**, 109290-1-11 (2021)
38. K. Terayama, K. Tsuda, R. Tamura, Jpn. J. Appl. Phys. **58**, 098001-1-4 (2019)
39. P. Amalthi, J. Judith Vijaya, L. John Kennedy, A. Mustafa, M. Bououdina, J. Phys. Chem. Solids **169**, 110860-1-17 (2022)
40. H. Yang, C. Han, X. Xue, J. Environ. Sci. **26**, 1489–1495 (2014)
41. N.S. Abdul Satar, R. Adnan, H.L. Lee, S.R. Hall, T. Kobayashi, M.H. Mohamad Kassim, K.N.H. Mohd, Ceram. Int. **45**, 15964–15973 (2019)
42. L. Wang, H. Gu, J. He, T. Zhao, X. Zhang, C. Xiao, H. Liu, X. Zhang, Y. Li, J. Alloys Compd. **695**, 599–606 (2017)